

Chainlike Mesoporous SnO<sub>2</sub> as a Well-Performing Catalyst for Electrochemical CO<sub>2</sub> Reduction

*Original*

Chainlike Mesoporous SnO<sub>2</sub> as a Well-Performing Catalyst for Electrochemical CO<sub>2</sub> Reduction / Bejtka, Katarzyna; Zeng, Juqin; Sacco, Adriano; Castellino, Micaela; Hernández, Simelys; Farkhondeh, M. Amin; Savino, Umberto; Ansaloni, Simone; Pirri, Candido F.; Chiodoni, Angelica. - In: ACS APPLIED ENERGY MATERIALS. - ISSN 2574-0962. - ELETTRONICO. - 2:5(2019), pp. 3081-3091. [10.1021/acsaem.8b02048]

*Availability:*

This version is available at: 11583/2734428 since: 2020-01-14T10:27:19Z

*Publisher:*

American Chemical Society

*Published*

DOI:10.1021/acsaem.8b02048

*Terms of use:*

This article is made available under terms and conditions as specified in the corresponding bibliographic description in the repository

*Publisher copyright*

(Article begins on next page)



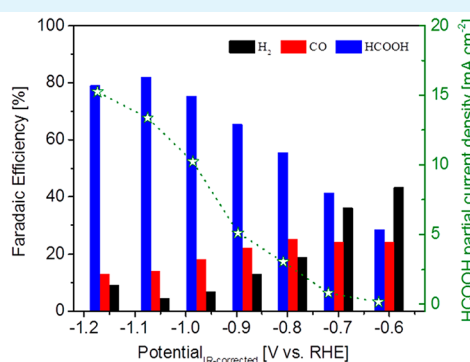
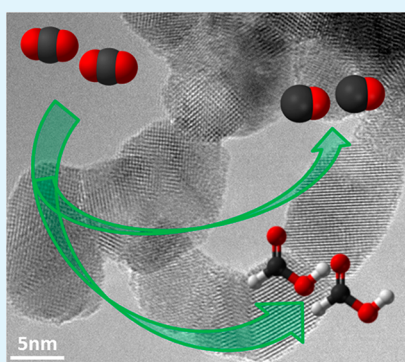
# Chainlike Mesoporous $\text{SnO}_2$ as a Well-Performing Catalyst for Electrochemical $\text{CO}_2$ Reduction

Katarzyna Bejtka,<sup>\*,†</sup> Juqin Zeng,<sup>\*,†</sup> Adriano Sacco,<sup>†</sup> Micaela Castellino,<sup>‡</sup> Simelys Hernández,<sup>†</sup> M. Amin Farkhondeh,<sup>†</sup> Umberto Savino,<sup>‡</sup> Simone Ansaloni,<sup>‡</sup> Candido F. Pirri,<sup>‡</sup> and Angelica Chiodoni<sup>†</sup>

<sup>†</sup>Center for Sustainable Future Technologies @ POLITO, Istituto Italiano di Tecnologia, Via Livorno 60, 10144 Turin, Italy

<sup>‡</sup>Department of Applied Science and Technology, Politecnico di Torino, Corso Duca degli Abruzzi 24, 10129 Turin, Italy

## S Supporting Information



**ABSTRACT:** In this Article, we present an easy, quick, and scalable route, based on anodic oxidation, for the preparation of mesoporous  $\text{SnO}_2$  as an efficient electrocatalyst for the  $\text{CO}_2$  reduction reaction ( $\text{CO}_2\text{RR}$ ). Crystallographically interconnected  $\text{SnO}_2$  nanocrystals with abundant grain boundaries, high specific surface area, and easily accessible porosity result to be active and selective for the  $\text{CO}_2\text{RR}$ . This electrocatalyst shows faradaic efficiency (FE) of about 95% at  $-0.97$  and  $-1.06$  V versus reversible hydrogen electrode (RHE) toward the formation of predominant  $\text{HCOOH}$  and minor  $\text{CO}$ . A peak FE value of 82% for the  $\text{HCOOH}$  production is obtained at  $-1.06$  V vs RHE. High  $\text{HCOOH}$  partial current densities of  $10.2$  and  $15.3$   $\text{mA cm}^{-2}$  are observed at  $-0.97$  and  $-1.15$  V vs RHE, respectively. Thorough electrochemical characterizations demonstrate that the synthesized  $\text{SnO}_2$ -based gas diffusion electrode allows efficient diffusion of  $\text{CO}_2$  even at high kinetics because of the highly open porous structure. The good understanding of the catalyst behavior is achieved also after the electrode testing, and it shows that the proposed preparation route results in a stable and durable material. The here reported promising results can be exploited for developing high-performance and sustainable electrocatalysts with a high potential to be implemented in real  $\text{CO}_2$  conversion devices.

**KEYWORDS:** electrochemical  $\text{CO}_2$  reduction,  $\text{SnO}_2$  catalyst, mesoporous,  $\text{HCOOH}$  production, anodic oxidation

## 1. INTRODUCTION

The production of carbon-based chemicals and fuels by exploiting anthropogenic  $\text{CO}_2$  is nowadays a topic of huge attention within the scientific community. Recently, we breached the 410 ppm threshold for atmospheric  $\text{CO}_2$ , after its previous alarming concentration of 400 ppm observed in 2013 and stabilized for good in 2017.<sup>1</sup> An advantageous method to reduce its concentration is to consider it as a valuable raw material. For instance, the  $\text{CO}_2$  electrochemical reduction can result in value-added products, while the energy needed for the process can be supplied by renewable energy sources.<sup>2</sup> Among many products that can be obtained, which depend on the catalyst characteristics, reaction conditions and electrolyte, the  $\text{CO}_2$  reduction reaction ( $\text{CO}_2\text{RR}$ ) to carbon monoxide ( $\text{CO}$ ) or formic acid ( $\text{HCOOH}$ ) is up to now the

economically most viable processes that can challenge conventional production routes.<sup>3</sup>  $\text{CO}$  can be converted to oxygenates and hydrocarbons through Fischer–Tropsch process.<sup>4,5</sup> Formic acid has a great range of applications, since it is a naturally occurring, environmentally benign organic acid used in agriculture and manufacturing. Moreover, its salts are used as deicing agents for airports, as heat transfer fluids, and in oil well drilling and finishing. Formic acid is also increasing its potential as hydrogen carrier and as fuel for fuel cells.<sup>6–10</sup>

**Received:** November 26, 2018

**Accepted:** April 5, 2019

**Published:** April 5, 2019



Tin oxide-based materials are known to catalyze the electrochemical reduction of  $\text{CO}_2$  to these two valuable products.<sup>11–17</sup> These materials are environmentally friendly and inexpensive. Their structure and morphology can play a decisive role in enhancing the catalytic properties. A great number of methods have been developed to prepare nanostructured  $\text{SnO}_2$  catalysts for  $\text{CO}_2$ RR, including hydrothermal synthesis,<sup>11–13</sup> aerogel,<sup>14</sup> solvo-plasma technique,<sup>15</sup> electrodeposition,<sup>16</sup> and electrostatic spinning.<sup>17</sup> Anodic oxidation (AO) of tin is a simple, high yield, low-cost, scalable, and effective strategy to prepare nanostructured porous  $\text{SnO}_2$  material,<sup>18</sup> with pore walls made of small interconnected nanoparticles (NPs), and with a high surface area. To the best of our knowledge, there are no reports on the application of anodized Sn for the  $\text{CO}_2$  electroreduction.

The interest in this material comes from the evidence that superior catalytic performances are observed in high-surface area materials like open or mesoporous structures because of easier access of the electrolyte to the catalytic sites and efficient mass diffusion.<sup>19–21</sup> Nanostructuring of the electrocatalysts with tailored surface configuration is an effective strategy to enhance their catalytic activity.<sup>15,22,23</sup> This was observed in various systems, and for example in precious metals, namely, Au and Cu, it was shown that broken spatial symmetry near grain boundaries (GB) changes the binding energy of the reaction intermediate facilitating the  $\text{CO}_2$  reduction to  $\text{CO}^{22}$  and  $\text{CO}$  reduction to  $\text{C}_2^+$  products.<sup>23</sup> In addition, in Sn-based catalyst, precisely potassium-rich tin oxide nanowires, it was observed that the creation of defects, including GBs, results in an enhanced catalytic activity toward  $\text{HCOOH}$  formation.<sup>15</sup>

Given these premises, it is strategic to develop nanostructured catalysts, which can be studied at a lab-scale level, by using a fabrication technique also applicable at industrial scale, and using low-cost raw materials. Here we report a facile, quick, and low-cost synthesis method of chainlike mesoporous  $\text{SnO}_2$  with rich grain boundaries, high specific surface area and large mesopore volume. The composition, morphology, crystal structure, and pore structure of the  $\text{SnO}_2$  nanocatalysts were characterized using scanning electron microscopy (SEM), transmission electron microscopy (TEM), X-ray diffraction (XRD), Raman, X-ray photoelectron spectroscopy (XPS), and  $\text{N}_2$  adsorption isotherm. Cyclic voltammetry, electrochemical impedance spectroscopy, and chronoamperometric measurements were conducted to elucidate the catalytic performance of the electrodes for the  $\text{CO}_2$ RR. Moreover, to evaluate the advantage of the proposed  $\text{SnO}_2$  preparation method and nanostructure, we compared the catalytic performance of the synthesized  $\text{SnO}_2$ -based electrode to that of a commercial  $\text{SnO}_2$  NPs-based electrode and of a Sn foil. It is important to study the catalyst not only before but also after it has worked, as this can help to optimize its durability and catalytic capability. Hence, stability tests and subsequent morphologic/structural changes were carefully studied. This work represents an important advancement toward understanding of the role of porosity and GB of the catalysts for enhanced catalytic performance.

## 2. EXPERIMENTAL SECTION

**2.1. Catalyst Preparation.** The nanostructured  $\text{SnO}_2$  was prepared by a one-step anodic oxidation method in a homemade two-electrode cell, using Sn foil (0.15 mm thick, purity 99.7%, Goodfellow) as the anode and a Pt foil as the cathode. Prior to anodization, the tin foils were ultrasonically cleaned in acetone and

ethanol and then dried in a  $\text{N}_2$  stream. The electrolyte used was a solution of  $\text{H}_2\text{O}$  and  $\text{NaOH}$  (0.3 M,  $\geq 98.0$  wt %, Sigma-Aldrich). The applied anodization voltage was 10 V, under continuous stirring in an ambient environment. The as-anodized samples were carefully rinsed with deionized water and dried with  $\text{N}_2$ . The samples were then annealed for 2 h in air at the lowest temperature necessary to obtain the tetragonal rutile  $\text{SnO}_2$  crystalline structure, that is, 450 °C.

**2.2. Electrode Preparation.** To prepare the  $\text{SnO}_2$ -based gas diffusion electrode (GDE), 10 mg of synthesized  $\text{SnO}_2$ , 1.5 mg of acetylene carbon black (CB, Shawinigan Black AB50), 90  $\mu\text{L}$  of Nafion 117 solution (5 wt %, Adrich), and 320  $\mu\text{L}$  of isopropanol (Sigma-Aldrich) were well mixed and sonicated for 30 min until a uniform slurry was obtained. The slurry was then coated onto a carbon paper gas diffusion layer (GDL; SIGRACET 28BC, SGL Technologies). The GDE was dried at 60 °C overnight to evaporate the solvents. The mass loading of  $\text{SnO}_2$  is about 3.0  $\text{mg cm}^{-2}$ . For comparison, a GDE containing commercial  $\text{SnO}_2$  (nanopowder no. 549657, Aldrich) was prepared with the same procedure and the same  $\text{SnO}_2$  loading. Thereafter the GDE with synthesized  $\text{SnO}_2$  is named  $\text{SnO}_2$ -anod and the one with commercial  $\text{SnO}_2$  is named  $\text{SnO}_2$ -comm. A Sn foil (thickness = 0.15 mm, purity = 99.7%, Goodfellow) was also used as a comparison electrode.

**2.3. Characterization.** Field-emission scanning electron microscopy (FESEM, ZEISS Auriga) was used to evaluate the morphology of the as-grown material and prepared electrodes. Samples for transmission electron microscopy (TEM) were prepared both by drop coating solution of obtained material dispersed in ethanol onto a holey carbon coated Cu grid and by standard lift-out technique by using Focused Ion Beam system (FIB, ZEISS Auriga). TEM observations were performed with a FEI Tecnai F20ST microscope, equipped with a field emission gun (FEG) operated at 200 kV. High-angle annular dark field (HAADF), bright field (BF), and energy dispersive X-ray spectroscopy (EDX, EDAX) detectors were used in scanning TEM (STEM) mode. X-ray diffraction (XRD) was performed in Bragg–Brentano symmetric geometry by using a PANalytical X'Pert Pro instrument (Cu  $K\alpha$  radiation, 40 kV and 30 mA) equipped with an X'Celerator detector. Brunauer–Emmett–Teller (BET) specific surface area, average pore size and total pore volume of the catalysts were measured via the  $\text{N}_2$  physisorption at  $-196$  °C (Micrometrics ASAP 2020). Prior to the analysis, the powders were outgassed at 200 °C for 2 h to remove water and atmospheric contaminants. X-ray photoelectron spectroscopy (XPS) was carried out by using a PHI 5000 VersaProbe (Physical Electronics) system. The X-ray source was a monochromatic Al  $K\alpha$  radiation (1486.6 eV). Spectra were analyzed using Multipak 9.7 software. All core-level peak energies were referenced to C 1s peak at 284.5 eV (C–C/C–H) and the background contribution in high-resolution (HR) scans was subtracted by means of a Shirley function. Raman spectroscopy was carried out with a Renishaw inVia Reflex micro-Raman spectrophotometer equipped with a cooled charge-coupled device camera and excited with a 514.5 nm wavelength solid-state laser source.

### 2.4. Electrochemical Tests and Reduction Product Analysis.

Before each electrochemical measurement, the electrode was in situ reduced at  $-1.0$  V vs RHE for 20 min until a constant current was achieved. Unless otherwise specified, in this work all the potentials refer to RHE. Cyclic voltammetry (CV) and electrochemical impedance spectroscopy (EIS) were performed in a three-electrode cell at room temperature with a CHI760D electrochemical workstation. The working electrode was a GDE with a geometric area of 0.2  $\text{cm}^2$ . A Pt wire was used as counter electrode and a Ag/AgCl (3 M NaCl) was used as reference electrode. To study the electrocatalytic performance of the electrodes, CV measurements were performed from 0.6 to  $-1.2$  V at a scan rate of 10  $\text{mV s}^{-1}$  in  $\text{N}_2$ - and  $\text{CO}_2$ -saturated 0.1 M  $\text{KHCO}_3$  aqueous solutions. EIS measurements were performed at various potentials from  $-1.3$  to  $-0.3$  V with an AC signal of 10 mV of amplitude and  $10^{-1}$ – $10^4$  Hz frequency range in  $\text{N}_2$ - and  $\text{CO}_2$ -saturated 0.1 M  $\text{KHCO}_3$  aqueous solutions. To determine the double-layer capacitance ( $C_{dl}$ ) of the electrodes, CVs were executed in a potential range between  $-0.29$  and  $-0.39$  V at



scan rates of 5, 10, 20, 30, 40, and 50 mV s<sup>-1</sup> in the CO<sub>2</sub>-saturated 0.1 M KHCO<sub>3</sub> aqueous solution.

The CO<sub>2</sub>RR experiments were conducted in a custom-made two-compartment cell with a proton exchange membrane (Nafion Membrane N117, Sigma-Aldrich) as the separator. The volume of each side was 40 mL with 15 mL of headspace. Chronoamperometric (CA) measurements were carried out by using a CHI760D electrochemical workstation, with Ag/AgCl (3 M NaCl) as the reference and a Pt coiled wire as the counter electrode. The working electrode was a GDE (SnO<sub>2</sub>-anod or SnO<sub>2</sub>-comm) with geometric area of 1.5 cm<sup>2</sup>. KHCO<sub>3</sub> aqueous solution (0.1 M) was used as electrolyte. Gas-phase products were analyzed online with a micro gas chromatograph ( $\mu$ GC, Fusion, INFICON) equipped with two channels with a 10-m Rt-Molsieve 5A column and an 8-m Rt-Q-Bond column, respectively, and microthermal conductivity detectors (micro-TCD). The inlet of the  $\mu$ GC equipment was connected to the cathodic side of the electrochemical cell through a GENIE filter to remove the humidity from the gas. During the CA measurements, a constant CO<sub>2</sub> flow rate of 20 mL min<sup>-1</sup> was maintained to saturate the electrolyte and to carry out the gaseous products to the  $\mu$ GC. Liquid products were analyzed by a high-performance liquid chromatograph (Shimadzu Prominence HPLC) with a Diode Array Detector (DAD) set at 210 nm by using a Rezex ROA (300  $\times$  7.8 mm) column, with 5 mM H<sub>2</sub>SO<sub>4</sub> (flow rate of 0.5 mL min<sup>-1</sup>) as mobile phase. The faradaic efficiency (FE) of each product was calculated by dividing the coulombs needed to produce the concentration of each product by the total coulombs during a corresponding reduction period.

For CV and CA experiments, the potential was corrected by compensating the ohmic potential drop, of which 85% by the technique in the instrument (*iR*-compensation) and 15% by manual calculation.

### 3. RESULTS AND DISCUSSION

**3.1. Characterization of the Prepared SnO<sub>2</sub> Nanocatalysts.** The morphology of the as-prepared SnO<sub>2</sub> can be seen in the FESEM image in Figure 1a and 1b. An irregular porous structure is observed from the top view image (Figure 1a), while nanochannels oriented along the growth direction,

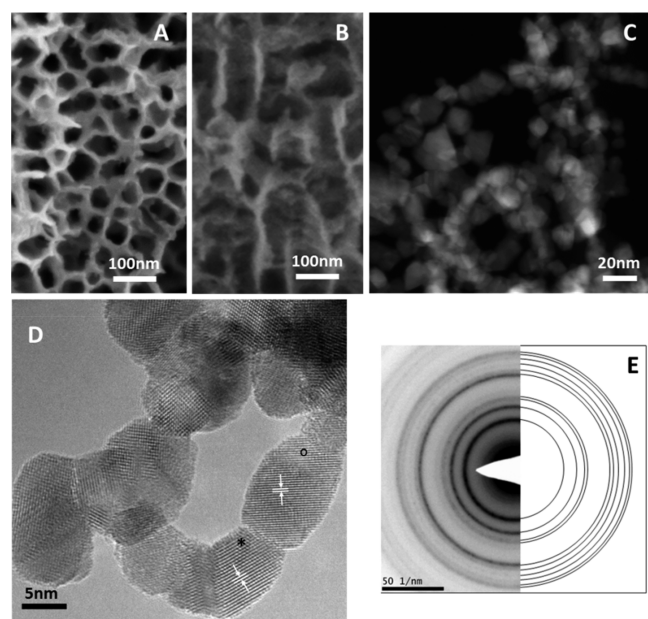


**Figure 1.** Electron microscopy characterization of the as-grown SnO<sub>2</sub>: (a, b) FESEM top and cross-section views, respectively, (c) STEM image, (d) HR-TEM image of the chain structure showing GBs, and (e) SAED.

with wall thickness of about 15 nm, are evidenced in the cross-section view (Figure 1b).<sup>18</sup> The pore structure is irregular, unlike the highly ordered structure that is obtained for other oxides prepared by the same growth method, like Al<sub>2</sub>O<sub>3</sub> or TiO<sub>2</sub>.<sup>24,25</sup> In Figure S1e, the morphology of the commercial SnO<sub>2</sub> is shown for comparison. It is characterized by round nanoparticles having different crystal size, in the range of 10–100 nm.

To better understand the pore structure of the as-prepared and commercial samples, N<sub>2</sub> sorption isotherm has been performed (Figure S2). SnO<sub>2</sub> obtained by anodic oxidation exhibits a specific surface area of 64.3 m<sup>2</sup> g<sup>-1</sup>, an average pore size of 25 nm, and a pore volume of 0.43 cm<sup>3</sup> g<sup>-1</sup>, while commercial SnO<sub>2</sub> exhibits a specific surface area of 31.5 m<sup>2</sup> g<sup>-1</sup>, an average pore size of 10 nm, and a pore volume of 0.08 cm<sup>3</sup> g<sup>-1</sup>. These findings put in evidence the higher availability of catalytic sites of here proposed SnO<sub>2</sub>-anod because of its higher surface area and porosity than the SnO<sub>2</sub>-comm, as also confirmed by the FESEM characterization.

TEM characterization was performed to study the crystalline structure in detail. STEM image (Figure 1c) reveals that the pore walls of the SnO<sub>2</sub> prepared via anodic oxidation consist of chainlike connected nanocrystals with a size in the range of 8–20 nm, which is in line with the FESEM observation. The high-resolution TEM (HRTEM) image (Figure 1d) gives more insight into the type of connection between the NPs and displays the interface between the neighboring SnO<sub>2</sub> nanocrystals. It is observed that the individual SnO<sub>2</sub> nanocrystallites are crystallographically interconnected to each other via grain boundaries. The large number of structural defects created by either local lattice strain or deviation of the atoms from their ideal positions, are generated at the sites of grain boundaries, which are believed to act as highly active sites for CO<sub>2</sub> reduction reaction.<sup>15,22,23</sup> As shown in Figure 1d the NPs themselves show a good crystallinity, with lattice fringes with regular spacings equal to 2.68 and 3.31 Å, which are consistent with interplanar distances of (101) and (110) planes of SnO<sub>2</sub>, respectively (tin oxide, JCPDS 00-041-1445). The selected area electron diffraction (SAED) pattern (Figure 1e) shows well-defined diffraction rings, confirming as HRTEM, polycrystalline SnO<sub>2</sub> (tin oxide, JCPDS 00-041-1445), with highly crystalline structure.

TEM image of commercial SnO<sub>2</sub> is shown in Figure S3 for comparison. The commercial nanopowder consists of many crystals with the diameter in the range of 5–100 nm. The HRTEM shows that these crystals are not crystallographically interconnected (as evidenced in Figure S3b by yellow arrows) and confirms their larger size. The larger size of the crystals results in lower surface area than SnO<sub>2</sub> prepared via anodic oxidation and the fact that the crystals are not interconnected results in a more compact structure, which is not as porous as that of anodic SnO<sub>2</sub>, in line with N<sub>2</sub> sorption isotherm results.

**3.2. Characterization of the GDEs.** The morphology of the as-prepared SnO<sub>2</sub>-anod electrode is shown in Figure 2a. It shows that the nanostructure of SnO<sub>2</sub> remains well preserved and mixed with carbon black and Nafion. A direct comparison between the electrode and the as-prepared catalyst is shown in Figure S1a and S1b, where both are reported at the same magnification. The catalyst in the electrode remains porous, and therefore the advantages that a porous catalyst can offer, including high surface area and easy access to active sites, are preserved. Figure S1 shows also the comparison of the SnO<sub>2</sub>-



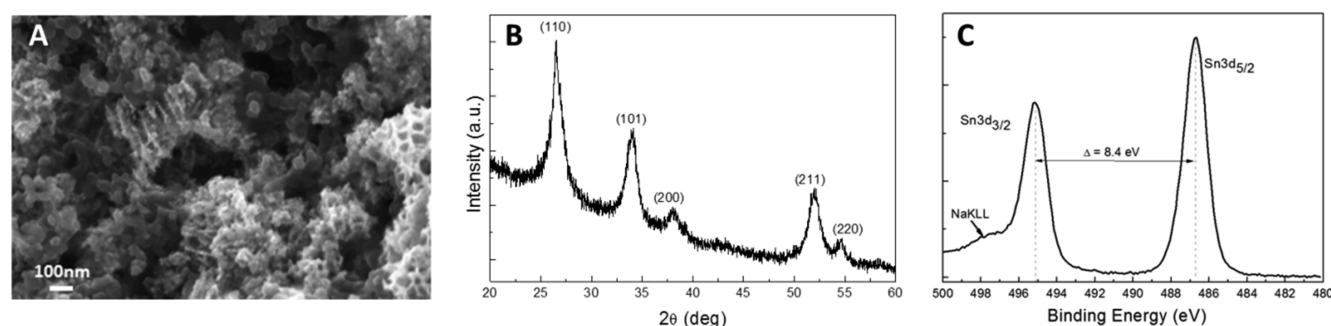


**Figure 2.** Characterization of SnO<sub>2</sub>-anod electrode: (a) FESEM image, (b) XRD pattern, and (c) XPS Sn 3d core level HR.

anod with the SnO<sub>2</sub>-comm electrode (Figure S1e). Also the latter catalyst is well dispersed within the electrode.

Crystalline phase and surface chemical composition of SnO<sub>2</sub>-anod electrode were examined by XRD, Raman spectroscopy and XPS. The XRD pattern (Figure 2b) of this electrode displays the main peaks for SnO<sub>2</sub> (tin oxide JCPDS 00-041-1445) crystalline phase. Peak shape gives evidence of small coherent diffraction domains, consistent with HRTEM analysis (Figure S6a). The same main peaks were observed in the pattern of SnO<sub>2</sub>-comm (Figure S4b). For this electrode, the peak width gives evidence of bigger crystals in the SnO<sub>2</sub>-comm than in the SnO<sub>2</sub>-anod, as also evident from the FESEM in Figure S1e and TEM in Figure S3.

Raman shift spectrum of SnO<sub>2</sub>-anod electrode (Figure S5) resembles the vibration modes of SnO<sub>2</sub>.<sup>26</sup> There are two main peaks at 631 and 775 cm<sup>-1</sup>, which can be assigned to A<sub>1g</sub> (symmetric Sn–O stretching) and B<sub>2g</sub> (asymmetric Sn–O stretching) vibration modes of SnO<sub>2</sub> crystallites, respectively.<sup>26</sup> The peaks positions are slightly shifted with respect to the bulk, as for small particles, A<sub>1g</sub> and B<sub>2g</sub> modes of SnO<sub>2</sub> are shifted to lower wavenumbers and E<sub>g</sub> mode is shifted to higher wavenumber.<sup>27</sup> These results show that the SnO<sub>2</sub>-anod possess the crystalline structure of the tetragonal rutile structure, which is in perfect agreement with the XRD results.

The chemical composition of the as-prepared electrode surface has been checked by means of XPS analysis. The survey scan, not reported, confirms the presence of Sn, F, C, O, and S, which are in accordance with the composition of the electrode. To obtain more information regarding the surface Sn oxidation state, a high resolution (HR) scan was performed and is reported in Figure 2c. The Sn 3d doublet has its Sn 3d<sup>5/2</sup> peak at 486.7 eV and the Sn 3d<sup>3/2</sup> peak at 495.1 eV, 8.4 eV apart from the first one, and can be ascribed to Sn(IV) as reported by B.K. Lee et al.<sup>28</sup>

**3.3. Electrochemical Behavior for CO<sub>2</sub> Electroreduction.** The electrodes were reduced in CO<sub>2</sub>-saturated 0.1 M KHCO<sub>3</sub> aqueous solution for 20 min at −1.0 V before each electrochemical measurement. The reductive current density initially decreases and then achieves a quasi-constant value.

The morphology and structure of SnO<sub>2</sub> based electrodes were investigated after the 20 min reduction step with FESEM and XRD, shown Figures 3 and S4, respectively. The FESEM images do not evidence any significant change in the morphology of the SnO<sub>2</sub>-based electrodes after this treatment.

However, the XRD patterns of both electrodes evidence presence of small amount of metallic Sn (tin, JCPDS 01-086-2265), in addition to the unaltered peaks of the SnO<sub>2</sub> (tin oxide, JCPDS 00-041-1445) crystalline phase. To investigate the proposed SnO<sub>2</sub>-anod electrode in more detail, the HRTEM

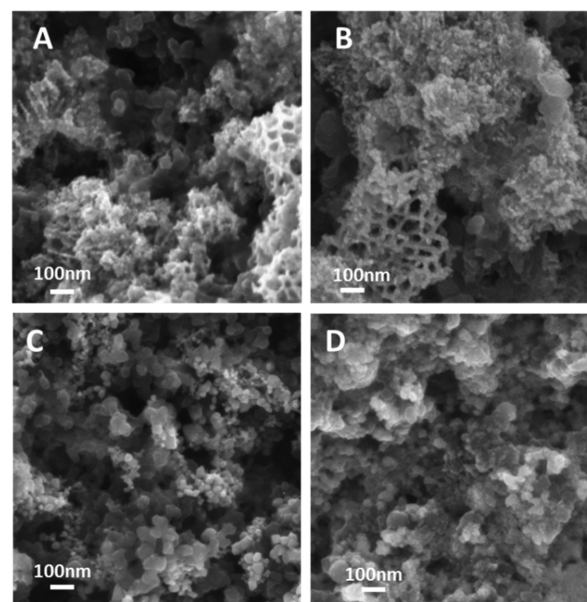


**Figure 3.** Top-view FESEM images of the anodic and commercial SnO<sub>2</sub> based electrodes: (a) as-prepared SnO<sub>2</sub>-anod electrode, (b) SnO<sub>2</sub>-anod electrode reduced for 20 min, (c) as-prepared SnO<sub>2</sub>-comm electrode, and (d) SnO<sub>2</sub>-comm electrode reduced for 20 min.

and STEM were also performed. These also confirm that after 20 min of the reduction process the electrode remains unaltered, as shown in Figure S6. In both the as-prepared and reduced electrodes the good crystallinity and crystals connections through grain boundaries are evidenced.

Besides the morphology and crystalline structure, evaluating the electrochemical active surface area (ECSA) is also of high importance in the investigation and development of electrodes.<sup>29</sup> The double-layer capacitance ( $C_{dl}$ ) value is widely used to evaluate the ECSAs of the electrodes.<sup>30,31</sup> In this work, because of the nature of the GDEs (with complex composition), we were not able to calculate their ECSAs from the  $C_{dl}$  values. However, we compared the ECSAs of the SnO<sub>2</sub>-anod with that of SnO<sub>2</sub>-comm and of a flat Sn foil. As shown in Figure S7, both GDEs have enhanced  $C_{dl}$  values if compared to the flat Sn foil. Furthermore, the SnO<sub>2</sub>-anod shows a higher  $C_{dl}$  (approximately 10.0 mF cm<sup>-2</sup>) compared to the SnO<sub>2</sub>-comm (7.3 mF cm<sup>-2</sup>), indicating a larger ECSA for the former. Since both GDEs have the same SnO<sub>2</sub>/CB/Nafion ratio, the higher ECSA of the SnO<sub>2</sub>-anod is likely due to highly accessible mesopores in the synthesized SnO<sub>2</sub>, as confirmed by the N<sub>2</sub> sorption isotherm in Figure S2,<sup>21</sup> resulting in good access to GB, which are believed to provide active sites for

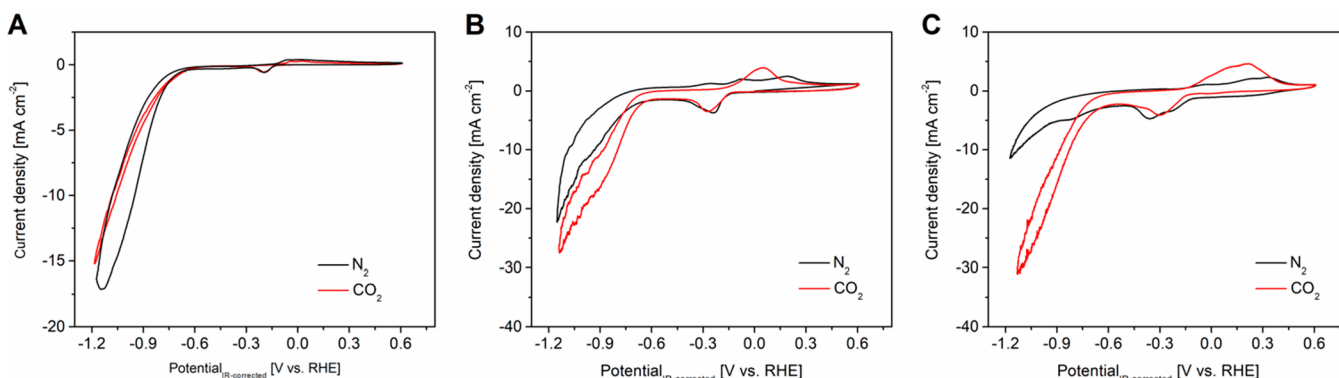


**Figure 4.** CVs on the three electrodes in  $N_2$ - and  $CO_2$ -saturated 0.1 M  $KHCO_3$  aqueous solutions at a scan rate of  $10 \text{ mV s}^{-1}$ : (a) Sn foil, (b)  $SnO_2$ -comm, and (c)  $SnO_2$ -anod.

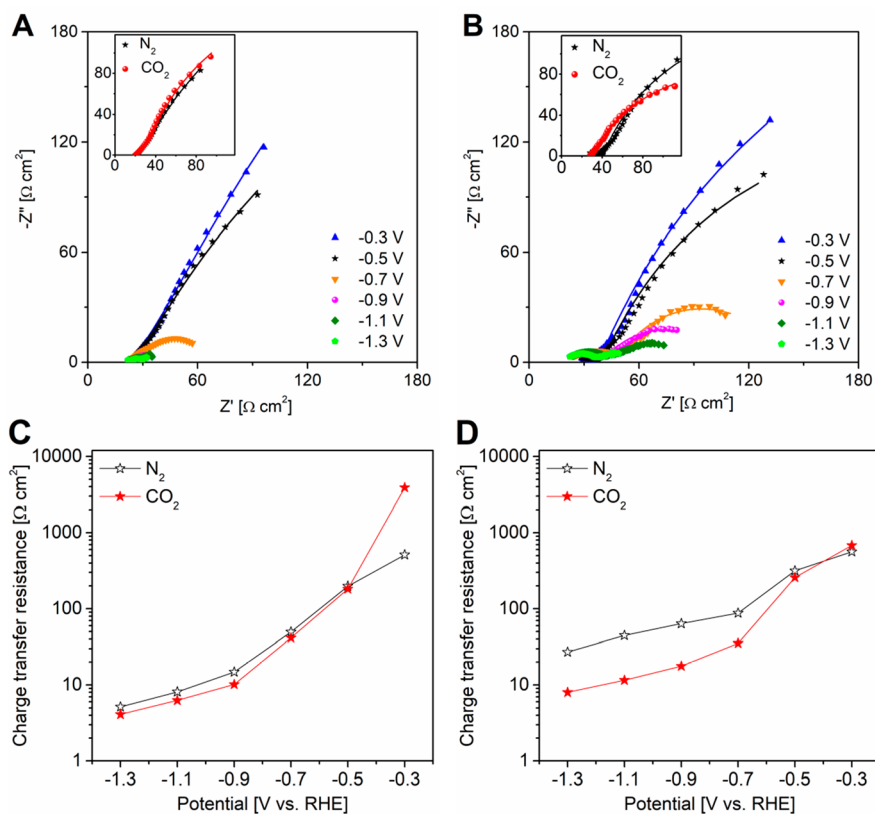


**Figure 5.** Nyquist plots obtained at different potentials in  $N_2$ -saturated electrolyte (the points are experimental data, and the lines are the curves calculated through fitting; in the inset, the two spectra acquired at  $-0.5 \text{ V}$  in  $N_2$ - and  $CO_2$ -saturated solutions are shown): (a)  $SnO_2$ -comm and (b)  $SnO_2$ -anod. Charge transfer resistances reported as a function of the potential: (c)  $SnO_2$ -comm and (d)  $SnO_2$ -anod.

$CO_2$  reduction.<sup>15</sup> This investigation implies that the  $SnO_2$ -anod could provide a larger number of active sites for the electrochemical reactions compared to the  $SnO_2$ -comm.

The electrocatalytic performance toward the  $CO_2RR$  of the  $SnO_2$ -based GDEs and Sn foil was first studied using CV in 0.1 M  $KHCO_3$  aqueous solution. Either  $N_2$  or  $CO_2$  gas was bubbled through the electrolyte for 30 min before CV tests and the same gas flux was maintained during the measurements. As shown in Figure 4, a set of redox peaks are observed with all the three electrodes in the potential range where no hydrogen evolution reaction (HER) and  $CO_2RR$  occur. The reduction peak from 0.0 to  $-0.4 \text{ V}$  is attributed to the reduction of Sn species and it couples to the reoxidation peak from 0.05 to  $0.5 \text{ V}$ .<sup>32</sup> In contrast with the Sn foil (Figure 4a), both  $SnO_2$

electrodes (Figure 4b and c) display higher geometric current densities in the  $CO_2$ -saturated electrolyte than in the  $N_2$  one at each applied potential below  $-0.8 \text{ V}$  vs RHE (where HER and  $CO_2RR$  likely happen). This opposite behavior indicates higher selectivity for the  $CO_2RR$  of the GDEs with respect to the Sn foil. When comparing the two GDEs in  $N_2$  electrolyte where only HER occurs, the  $SnO_2$ -anod (Figure 4c) shows a much lower geometric current density with respect to the  $SnO_2$ -comm (Figure 4b). Considering that the  $SnO_2$ -anod has a slightly higher ECSA than the  $SnO_2$ -comm, a much lower geometric current density suggests a lower intrinsic activity of the former toward the HER.

The voltammograms of the two GDEs in the  $CO_2$ -saturated electrolyte are compared in Figure S8. Similar behaviors can be

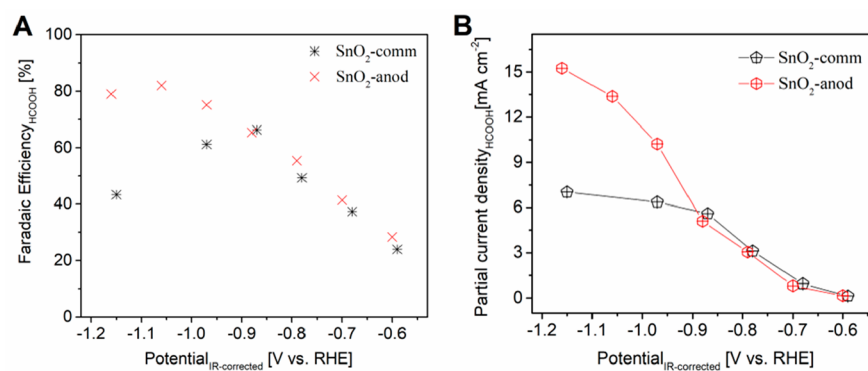


**Figure 6.** Performance of SnO<sub>2</sub>-comm and SnO<sub>2</sub>-anod electrodes for the CO<sub>2</sub>RR at various potentials: (a) Faradaic efficiencies for HCOOH formation and (b) HCOOH partial current densities.

observed at the two electrodes at high potentials ( $> -0.9$  V). At potentials lower than  $-0.9$  V, the SnO<sub>2</sub>-comm is likely suffering from mass diffusion limit, since a shoulder peak is observed. On the contrast, the SnO<sub>2</sub>-anod continues to quickly increase in the current density with decreasing the potential down to  $-1.2$  V. The different behavior of the two electrodes at high overpotentials implies that SnO<sub>2</sub>-anod is more effective in mass diffusion, probably due to the higher accessibility of CO<sub>2</sub> to the mesopores in the anodized SnO<sub>2</sub>.<sup>33</sup>

The results of CV characterization were successfully confirmed by electrochemical impedance spectroscopy (EIS) analysis. In Figures S9a and S9b and S9a, the Nyquist plots related to the measurements acquired for SnO<sub>2</sub>-comm, SnO<sub>2</sub>-anod, and Sn foil, respectively, at different potentials in N<sub>2</sub>-saturated 0.1 M KHCO<sub>3</sub> aqueous solution are reported. Similar curves were collected in CO<sub>2</sub>-saturated electrolyte (data not shown). As can be clearly seen, all the samples exhibit a reduction of the total impedance while decreasing the applied potential, in agreement with the current density trend in cyclic voltammograms reported in Figure 4. In addition, two main features can be distinguished in the Nyquist plots related to SnO<sub>2</sub> GDEs: a small high-frequency arc, which is related to the charge transport properties of the catalyst, and a large (incomplete) arc, which is associated with the charge transfer at catalyst/electrolyte interface.<sup>34</sup> These features are not clearly visible in the plot of Sn foil, since the large arc mask the high-frequency one, especially at high potentials. Moreover, it has to be highlighted that no mass diffusion component is visible in the impedance spectra of the three electrodes, due to low-frequency limitation.<sup>35</sup> In order to quantitatively analyze the two processes described above, EIS data were fitted with an equivalent circuit (Figure S10), composed by a resistance/capacitance parallel for each process and a series resistance, accounting for the contact and electrolyte resistances;<sup>36</sup> the calculated curves are reported in Figures S9a and S9b superimposed to the experimental ones. For what concerns the series and charge transport resistances, their values are found to be in the range 20–30 and 5–7  $\Omega$  cm<sup>2</sup>, respectively, for the three electrodes, with negligible dependence on the applied potential or gas saturating the electrolyte. On the other hand, the values of the charge transfer resistances obtained in the N<sub>2</sub> and CO<sub>2</sub> electrolyte are compared in Figure S9c and S9d for SnO<sub>2</sub>-comm and SnO<sub>2</sub>-anod, respectively. At potentials higher than  $-0.5$  V, the resistance values related to both solutions are quite similar for both GDEs, as easily understood from CV analysis (Figure 4). On the contrary, at lower

potentials, that is, when HER and CO<sub>2</sub>RR take place, a decisive reduction of the charge transfer resistance in CO<sub>2</sub>-saturated solution can be appreciated for SnO<sub>2</sub>-anod (as it is also evident by comparing the two Nyquist spectra reported in the inset of Figure S9b), while this difference is less apparent for SnO<sub>2</sub>-comm. Such an outcome implies that both SnO<sub>2</sub>-anod and SnO<sub>2</sub>-comm electrodes would have a promising selectivity for the CO<sub>2</sub>RR even if the former would obtain superior performance with respect to the latter. Opposite behavior is exhibited on the Sn foil, since lower charge transfer resistance was obtained in N<sub>2</sub>-saturated electrolyte. This result implies scarce activity of Sn foil toward the CO<sub>2</sub>RR.

To compare the performance of the two SnO<sub>2</sub> GDEs toward the CO<sub>2</sub>RR, CA measurements were carried out in CO<sub>2</sub>-saturated 0.1 M KHCO<sub>3</sub> aqueous solution in a two-compartment cell, at different applied potentials. As shown in Figure S11a and S11b, the current density is rather low at about  $-0.6$  V and it increases with decreasing the applied potential on both SnO<sub>2</sub>-anod and SnO<sub>2</sub>-comm. A remarkable raise of current density is observed at about  $-0.8$  V on both electrodes. A big difference in the behavior of the two GDEs emerges at about  $-0.9$  V and it can be observed at lower potentials. Compared to the SnO<sub>2</sub>-comm, the SnO<sub>2</sub>-anod electrode displays a much higher current density at  $-0.97$  V and it maintains this advantage at more negative potentials, as clearly shown in Figure S11c. Since HCOOH is the predominant product, we use it as an indicator to compare the performance of the two GDEs toward the CO<sub>2</sub>RR. The FEs and partial current densities for the HCOOH production at various potentials are shown in Figures 6a and 6b, respectively. With decreasing the potential, the FE<sub>HCOOH</sub> on the SnO<sub>2</sub>-anod demonstrates a quasi-steady increase down to  $-1.06$  V and then a slight decrease at  $-1.15$  V, with a peak value of 82% at  $-1.06$  V.

The HCOOH partial current density on the SnO<sub>2</sub>-anod increases continuously with lowering the potential and a maximum HCOOH partial current density of 15.3 mA cm<sup>-2</sup> is observed at  $-1.15$  V. The SnO<sub>2</sub>-comm shows similar behavior for the HCOOH production from  $-0.6$  to  $-0.88$  V, while presents a big difference at lower potentials. Negatively shifting the potential ( $< -0.88$  V) on the SnO<sub>2</sub>-comm, FE<sub>HCOOH</sub> decreases quickly down to 43% at  $-1.15$  V and HCOOH partial current density achieves a quasi-plateau of 7.0 mA cm<sup>-2</sup>. Combining this findings with aforementioned CVs (Figure 4), it is suggested that the SnO<sub>2</sub>-comm suffers much severe mass diffusion limits than the SnO<sub>2</sub>-anod. Considering that the



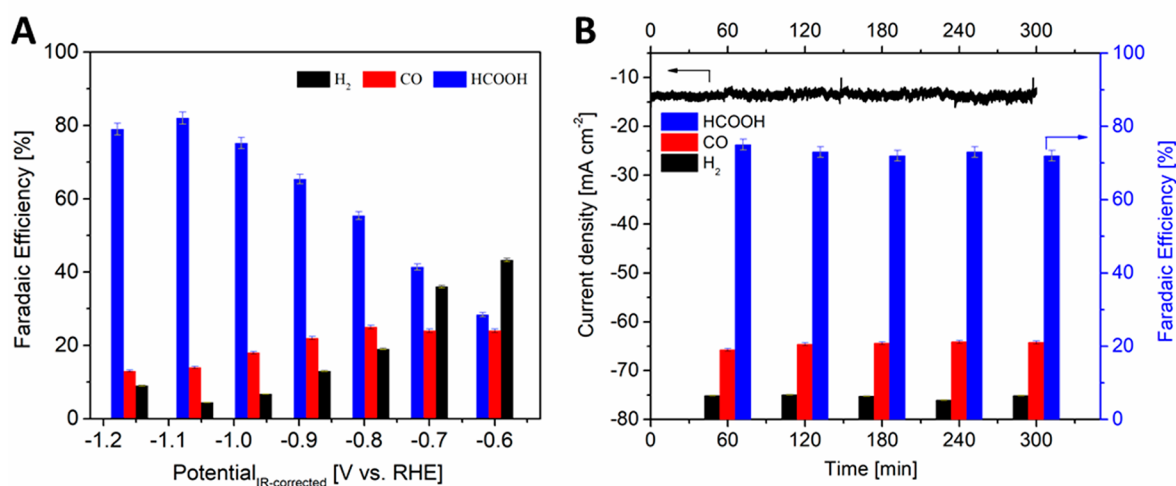


**Figure 7.** (a) Faradaic efficiencies for CO, HCOOH, and H<sub>2</sub> formation on the SnO<sub>2</sub>-anod electrode at various potentials and (b) five-hour electrolysis of CO<sub>2</sub> on SnO<sub>2</sub>-anod electrode at -0.97 V vs RHE in CO<sub>2</sub>-saturated 0.1 M KHCO<sub>3</sub> aqueous electrolyte.

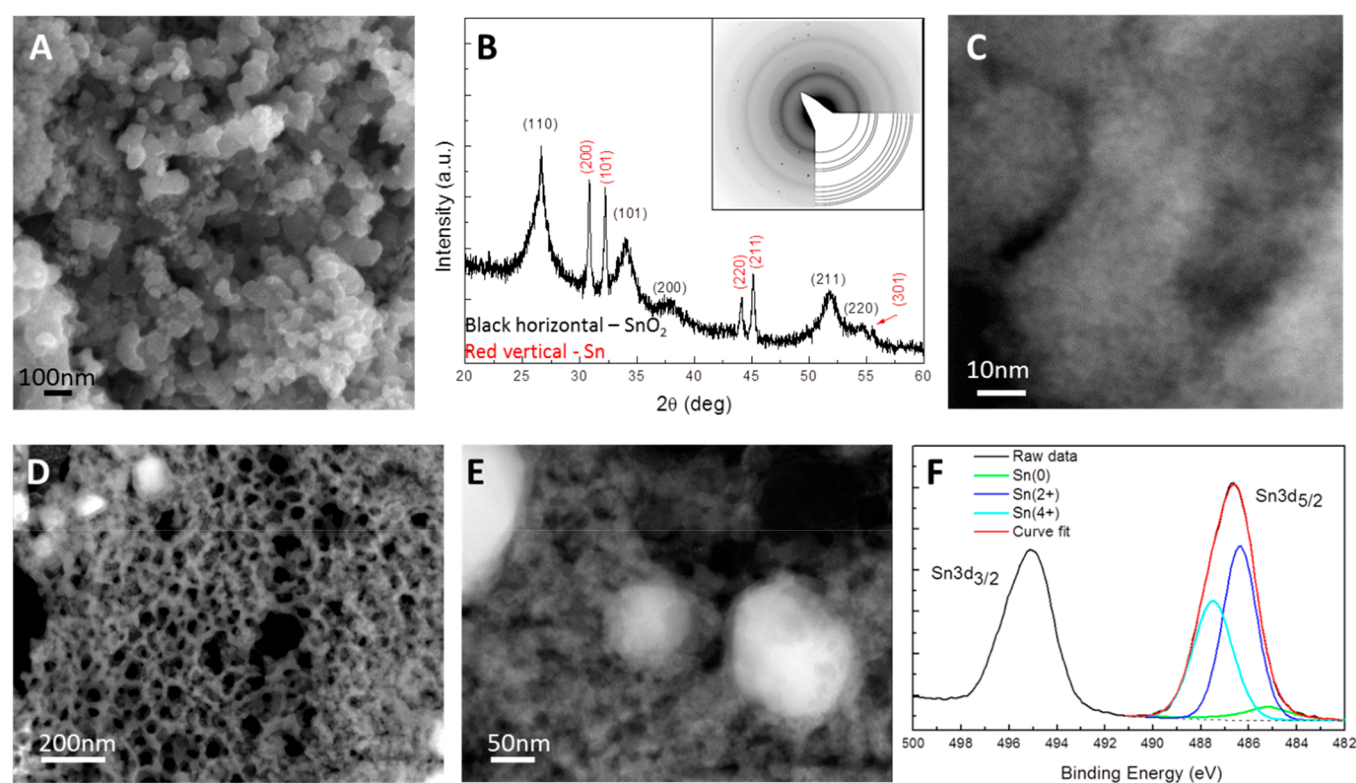


**Figure 8.** Characterization of the SnO<sub>2</sub>-anod electrode after 12 h of electrolysis: (a) top-view FESEM image, (b) XRD pattern with SAED in the inset, (c) HAADF-STEM image of some SnO<sub>2</sub> nanoparticles, (d and e) STEM-HAADF images of the cross section lamella, showing Sn particle immersed in the SnO<sub>2</sub> matrix, and (f) XPS Sn 3d doublet, showing three different oxidation states for Sn, as reported in the graph.

limitations could be attributed to mass diffusions of charges and CO<sub>2</sub> reactant, we compared the charge transfer resistance obtained from EIS on the two electrodes at various potentials, as shown in Figure S12. It is interesting to note that the SnO<sub>2</sub>-comm possesses almost half of the charge transfer resistance with respect to the SnO<sub>2</sub>-anod at low potentials from -0.9 to -1.3 V. Hence, the severe mass diffusion limits on the SnO<sub>2</sub>-comm should be related to poor availability of CO<sub>2</sub> at the active sites. Because of the depletion of CO<sub>2</sub> at active sites, the activity and selectivity for the CO<sub>2</sub>RR are dramatically inhibited and the HER becomes predominant at high kinetics,

as observed in our previous works.<sup>37,38</sup> On the contrary, a large number of mesopores in the SnO<sub>2</sub>-anod can provide highly accessible active sites and efficient mass diffusion, enhancing the catalytic performance especially at high kinetics.<sup>20</sup> In Tafel plot analysis (Figure S13), similar slopes are observed for HCOOH production on both SnO<sub>2</sub>-comm and SnO<sub>2</sub>-anod, which agrees with the EIS results at this potential range (Figure S12). These Tafel slopes are consistent with CO<sub>2</sub> reduction mechanisms that proceed through an initial rate-determining step of one electron transfer to CO<sub>2</sub>. The first electron transfer reaction is the formation of radical anion

$\text{CO}_2^-$ .<sup>39</sup> The  $\text{CO}_2^-$  formation is not easy since high energy is required for the reorganization between linear molecule and bent radical anion. This could be the reason for the poor performance of both  $\text{SnO}_2$  electrodes for converting  $\text{CO}_2$  to  $\text{HCOOH}$  at high potentials ( $>-0.7$  V,  $\text{FE}_{\text{HCOOH}} < 50\%$ ). At more negative potentials ( $-0.7$  to  $-0.9$  V for  $\text{SnO}_2$ -comm and  $-0.7$  to  $-1.1$  V for  $\text{SnO}_2$ -anod), more  $\text{CO}_2^-$  can be formed and consequently the  $\text{HCOOH}$  production is increased. Further decreasing potentials can introduce mass diffusion problem and thus favors other reaction pathways ( $<-0.9$  V for  $\text{SnO}_2$ -comm and  $-1.1$  V for  $\text{SnO}_2$ -anod).

To further study the behavior of  $\text{SnO}_2$ -anod for the  $\text{CO}_2\text{RR}$ , we report hereafter the complete analysis of the products, as well as the stability test, that have been conducted on this electrode. From Figure 7a, it is observed that the  $\text{CO}_2\text{RR}$  outcompetes the HER in all the tested potential range. The FE value for  $\text{H}_2$  evolution is about 40% from  $-0.6$  to  $-0.7$  V, and it reduces to about 16% from  $-0.8$  to  $-0.9$  V. With further decreasing the potential, the FEs for the HER reach values lower than 10%. The FE for CO production oscillates from 13% to 25% in the tested potential range. The  $\text{CO}_2\text{RR}$ , including CO and  $\text{HCOOH}$  production, achieves an excellent FE of 95% and a geometric current density of  $15.5 \text{ mA cm}^{-2}$  at  $-1.06$  V. As far as we know, such high selectivity and current density for the  $\text{CO}_2\text{RR}$  are comparable to the best results reported in other similar works at comparable potentials, as shown in Table S1. It is important to note that high selectivity and good current density are obtained at relatively low overpotentials, which is of huge importance for practical applications, as relatively low overpotentials result in energy savings to run the process and are required for direct utilization of renewable energy sources for driving the reaction, as for example photovoltaic, which is essential to achieve a carbon-even product.

The stability of the catalyst is as important as its activity and selectivity. Electrolysis of 5 h was carried out at  $-0.97$  V vs RHE to study the stability of the  $\text{SnO}_2$ -anod. As shown in Figure 7b, the geometric current density maintains a quasi-constant value of  $13.6 \text{ mA cm}^{-2}$ . The FE for  $\text{H}_2$  evolution maintains as low as 6–7% and CO yield remains quasi-constant at a FE value of about 20%. The selectivity for  $\text{HCOOH}$  oscillates between 72% and 75% during the electrolysis. Before this test, the electrode was tested for about 7 h under different conditions. Hence, a high stability of the electrode has been assessed for at least 12 h of operation.

**3.4. Structural and Morphological Characterization of Tested  $\text{SnO}_2$ -anod.** The morphology, phase changes, and crystallinity of the  $\text{SnO}_2$ -anod were studied via electron microscopy, XRD, Raman, and XPS also after 12 h of  $\text{CO}_2$  electrolysis.

Morphological characterization, shown in Figure 8a, evidence that the top surface the  $\text{SnO}_2$  electrode has changed during the long-term testing. The catalyst nanoparticles appear larger than the original nanoparticles (25–35 vs 8–20 nm, respectively). This suggests that during the electroreduction process they have tendency to recrystallize or aggregate into larger particles. To facilitate the comparison, Figure S1 shows FESEM images of the as prepared material, the as prepared electrode, the electrode after 20 min reduction, and the electrode after 12 h testing.

XRD measurement was performed to further investigate this change as well as to study the overall structural properties of the tested material. The diffraction peaks in the XRD graph of

the tested electrode, shown in Figure 8b, belong to  $\text{SnO}_2$  (tin oxide, JCPDS 00-041-1445) and metallic Sn (tin, JCPDS 01-086-2265) crystalline phases. This shows that part of  $\text{SnO}_2$  nanoparticles remain oxidized under the electrocatalytic conditions, and some  $\text{SnO}_2$  are reduced, which is consistent with previous studies.<sup>40,41</sup> The Sn peaks are very narrow, suggesting that large crystals were grown.

We also performed the estimation of the change of the crystallite size diameter of  $\text{SnO}_2$  using Scherrer's equation,<sup>42</sup> with fwhm calculated by fitting of the appropriate XRD reflection with PEARSON VII type function. It was found that there is indeed a decrease of the coherent diffraction domain size of about 12%. On the basis of the FESEM and XRD observations, we concluded that the size of the original crystallites (coherent diffraction domains) decreases, while they aggregate in bigger particles.

The Raman spectrum (Figure S14) of the tested electrode contains the previously observed vibrations, however their intensity is significantly decreased, which can suggest that the  $\text{SnO}_2$  was partially reduced to metallic tin which is Raman inactive,<sup>26,40</sup> in agreement with XRD results.

To better understand the XRD and FESEM results, the TEM characterization was performed. HAADF STEM in Figure 8c gives more insight into the change of the structure and morphology of the tested  $\text{SnO}_2$ -anod (also shown in Figure S6 together with characterization of the as-prepared and reduced for 20 min electrode), and evidence that the particles consist of very small (few nanometers) coherent diffraction domains. This characterization was performed on the material scratched from the tested electrode and represents its superior part. In addition, the TEM in the cross-section was performed in order to understand the characteristics of Sn particles within the porous structure. A TEM lamella extracted from the tested electrode was prepared by the standard lift-out FIB procedure. The STEM images of the lamella cross-section in Figure 8d and 8e show the representative part of the material. They evidence that the major part of the material retains its original morphology, and the chain-like connected NPs are still present. However, there are also areas where the nano-structured  $\text{SnO}_2$  was modified and large particles are observed. The EDX performed as a point measurement in and out of the large particle shows that the particle consists of Sn only, while other elements are observed outside (data reported in Figure S15). TEM (Figure S6c) also confirms that the size of the original crystallites decreases while they aggregate in bigger particles. SAED pattern of this sample (shown in inset of Figure 8b) shows a ring pattern, corresponding to  $\text{SnO}_2$ , and many spots, corresponding to large particles observed, confirming metallic Sn, in agreement with the XRD data.

XPS analysis also evidenced the appearance of new oxidation states for the Sn, since an enlargement in the peak fwhm has been noticed after the electrochemical test. In Figure 8f the Sn 3d doublet has been reported. A deconvolution procedure has been applied only to the Sn  $3d_{5/2}$  peak, for the sake of simplicity. Three curves have been overlapped to reproduce the raw data: one, asymmetric, at 485.2 eV for metallic Sn, another one at 486.3 eV for Sn(II) and the last one at 487.5 eV for Sn(IV). The chemical shift due to tin oxide is sometimes quite difficult to be ascribed to, since Sn(II) and Sn(IV) are usually quite close to each other, as reported by many authors.<sup>43,44</sup> In the as-prepared electrode, the Sn signal was quite sharp and only one component was sufficient to overlap the raw data by the curve fit. In the tested sample, the surface

has been modified by the chemical processes occurred. The appearance of defects and new chemical states has changed the overall surface oxidation state. The chemical shift of the Sn(IV) component toward higher binding energies has been also reported by N. R. Elezovic et al.<sup>45</sup> Therefore, we can conclude in accordance with the morphological and structural analysis, that apart from the SnO<sub>2</sub>, metallic tin is present in the tested sample. The presence of SnO is not confirmed by other investigation techniques. However, based on the above-mentioned ex situ techniques, we do not exclude the possibility that at the surface there is SnO. Recent work revealed that the Sn (II) is formed at those potentials that correspond to the maximum FE for HCOOH production, using operando or in situ approaches, such as Raman spectroscopy, X-ray absorption spectroscopy (XAS), and attenuated total reflection surface enhanced infrared adsorption spectroscopy (ATR-SEIRAS).<sup>46,47</sup>

#### 4. CONCLUSIONS

In summary, we have developed a highly efficient and stable SnO<sub>2</sub> catalyst for the electrochemical reduction of CO<sub>2</sub>. The highly crystalline SnO<sub>2</sub> is composed of nanoparticles with 8–20 nm in size. These particles are crystallographically interconnected to create a large number of grain boundaries. The SnO<sub>2</sub> has a mesoporous structure with a high specific surface area of 64.3 cm<sup>2</sup> g<sup>-1</sup> and a large pore volume of 0.43 cm<sup>3</sup> g<sup>-1</sup>. The anodic SnO<sub>2</sub>-based gas diffusion electrode has demonstrated excellent selectivity especially at high reaction rates toward the CO<sub>2</sub> reduction reaction because of rich active sites and facilely accessible porosity. The high performance of the electrode is largely maintained during an electrolysis period of 5 h. The tested electrode was characterized after cycling, evidencing some structural changes, including reduction of the coherent diffraction domains size, and their agglomeration into bigger particles at the surface, and appearance of large Sn crystals within all section of the electrode. This, however, did not affect the high selectivity and high activity of the electrode. The good understanding of the material and its characteristics both before and after the tests is of high importance for further work on catalyst improvement, through doping with elements which are predicted to further reduce the overpotentials for CO<sub>2</sub>RR.<sup>48</sup> In addition, since the selected anodic oxidation preparation route is scalable technique, it opens very interesting scenarios for real applications.

#### ■ ASSOCIATED CONTENT

##### Supporting Information

The Supporting Information is available free of charge on the ACS Publications website at DOI: 10.1021/acsae.8b02048.

Top-view FESEM images of the as-grown SnO<sub>2</sub>, as-prepared electrodes, electrodes reduced for 20 min, tested electrodes; N<sub>2</sub> adsorption/desorption isotherms for SnO<sub>2</sub> prepared via anodic oxidation and commercial; TEM image of the commercial SnO<sub>2</sub>; XRD patterns of SnO<sub>2</sub>-anod and SnO<sub>2</sub>-comm electrodes; Raman spectrum of as-prepared SnO<sub>2</sub>-anod electrode; TEM study of the crystals evolution of the SnO<sub>2</sub>-anod; determination of double-layer capacitance for various electrodes; comparison of the voltammograms of SnO<sub>2</sub>-comm and SnO<sub>2</sub>-anod in the CO<sub>2</sub> electrolyte; EIS analysis on a Sn foil electrode; equivalent circuit used for fitting of EIS data; CA measurements carried out on various electro-

des in CO<sub>2</sub>-saturated 0.1 M KHCO<sub>3</sub> aqueous solution at different potentials; comparison of charge transfer resistance obtained from EIS on SnO<sub>2</sub>-comm and SnO<sub>2</sub>-anod electrodes at various potentials; Tafel plot analysis for HCOOH production on SnO<sub>2</sub>-comm and SnO<sub>2</sub>-anod electrodes; Raman spectrum of tested SnO<sub>2</sub>-anod electrode; STEM image of the cross section lamella of tested SnO<sub>2</sub>-anod electrode; and comparison of electrocatalytic performance for reducing CO<sub>2</sub> to formic acid/formate on tin-based catalysts (PDF)

#### ■ AUTHOR INFORMATION

##### Corresponding Authors

\*E-mail: katarzyna.bejtka@iit.it.

\*E-mail: juqin.zeng@iit.it.

##### ORCID

Katarzyna Bejtka: 0000-0003-1731-5861

Juqin Zeng: 0000-0001-8885-020X

Adriano Sacco: 0000-0002-9229-2113

Simelys Hernández: 0000-0002-6722-0273

##### Notes

The authors declare no competing financial interest.

#### ■ ACKNOWLEDGMENTS

The authors thanks Hilmar Guzman and Marco Armandi for their support in BET characterization. This project has received funding from the European Union's Horizon 2020 Research and Innovation Programme under the Project RECODE (Grant Agreement No. 768583). The content of this publication is the sole responsibility of the authors. The European Commission or its services cannot be held responsible for any use that may be made of the information it contains.

#### ■ REFERENCES

- (1) <https://www.esrl.noaa.gov/gmd/ccgg/trends/> (accessed November 26, 2018).
- (2) Parajuli, R.; Gerken, J. B.; Keyshar, K.; Sullivan, I.; Sivasankar, N.; Teamey, K.; Stahl, S. S.; Cole, E. B. Integration of Anodic and Cathodic Catalysts of Earth-Abundant Materials for Efficient, Scalable CO<sub>2</sub> Reduction. *Top. Catal.* **2015**, *58*, 57–66.
- (3) Durst, J.; Rudnev, A.; Dutta, A.; Fu, Y.; Herranz, J.; Kaliginedi, V.; Kuzume, A.; Permyakova, A. A.; Paratcha, Y.; Broekmann, P.; Schmidt, T. J. Electrochemical CO<sub>2</sub> Reduction - A Critical View on Fundamentals, Materials and Applications. *Chimia* **2015**, *69* (12), 769–776; Jouny, M.; Luc, W.; Jiao, F. General Techno-Economic Analysis of CO<sub>2</sub> Electrolysis Systems. *Ind. Eng. Chem. Res.* **2018**, *57*, 2165–2177.
- (4) Kortlever, R.; Shen, J.; Schouten, K. J. P.; Calle-Vallejo, F.; Koper, M. T. M. Catalysts and Reaction Pathways for the Electrochemical Reduction of Carbon Dioxide. *J. Phys. Chem. Lett.* **2015**, *6*, 4073–4082.
- (5) Hernandez, S.; Amin Farkhondeh, M.; Sastre, F.; Makkee, M.; Saracco, G.; Russo, N. Syngas Production from Electrochemical Reduction of CO<sub>2</sub> Current Status and Prospective Implementation. *Green Chem.* **2017**, *19*, 2326–2346.
- (6) Yuranov, I.; Autissier, N.; Sordakis, K.; Dalebrook, A. F.; Grasmann, M.; Orava, V.; Cendula, P.; Gubler, L.; Laurenczy, G. Heterogeneous Catalytic Reactor for Hydrogen Production from Formic Acid and Its Use in Polymer Electrolyte Fuel Cells. *ACS Sustainable Chem. Eng.* **2018**, *6*, 6635–6643.
- (7) Perez-Fortes, M.; Schoneberger, J. C.; Boulamanti, A.; Harrison, G.; Tzimas, E. Formic acid synthesis using CO<sub>2</sub> as raw material:



Techno-economic and environmental evaluation and market potential. *Int. J. Hydrogen Energy* **2016**, *41*, 16444–16462.

(8) Eppinger, J.; Huang, K.-W. Formic Acid as a Hydrogen Energy Carrier. *ACS Energy Lett.* **2017**, *2*, 188–195.

(9) Onishi, N.; Laurenczy, G.; Beller, M.; Himeda, Y. Recent progress for reversible homogeneous catalytic hydrogen storage in formic acid and in methanol. *Coord. Chem. Rev.* **2018**, *373*, 317–332.

(10) Sordakis, K.; Tang, C.; Vogt, L. K.; Junge, H.; Dyson, P. J.; Beller, M.; Laurenczy, G. Homogeneous Catalysis for Sustainable Hydrogen Storage in Formic Acid and Alcohols. *Chem. Rev.* **2018**, *118*, 372–433.

(11) Zhang, S.; Kang, P.; Meyer, T. J. Nanostructured Tin Catalysts for Selective Electrochemical Reduction of Carbon Dioxide to Formate. *J. Am. Chem. Soc.* **2014**, *136*, 1734–1737.

(12) Li, F.; Chen, L.; Knowles, G. P.; MacFarlane, D. R.; Zhang, J. Hierarchical Mesoporous SnO<sub>2</sub> Nanosheets on Carbon Cloth: A Robust and Flexible Electrocatalyst for CO<sub>2</sub> Reduction with High Efficiency and Selectivity. *Angew. Chem., Int. Ed.* **2017**, *56*, 505–509.

(13) Li, Y.; Qiao, J.; Zhang, X.; Lei, T.; Girma, A.; Liu, Y.; Zhang, J. Rational Design and Synthesis of SnO<sub>x</sub> Electrocatalysts with Coralline Structure for Highly Improved Aqueous CO<sub>2</sub> Reduction to Formate. *ChemElectroChem* **2016**, *3*, 1618–1628.

(14) Yu, J.; Liu, H.; Song, S.; Wang, Y.; Tsiakaras, P. Electrochemical reduction of carbon dioxide at nanostructured SnO<sub>2</sub>/carbon aerogels: The effect of tin oxide content on the catalytic activity and formate selectivity. *Appl. Catal., A* **2017**, *545*, 159–166.

(15) Kumar, B.; Atla, V.; Brian, J. P.; Kumari, S.; Nguyen, T. Q.; Sunkara, M.; Spurgeon, J. M. Reduced SnO<sub>2</sub> Porous Nanowires with a High Density of Grain Boundaries as Catalysts for Efficient Electrochemical CO<sub>2</sub>-into-HCOOH Conversion. *Angew. Chem., Int. Ed.* **2017**, *56*, 3645–3649.

(16) Won, D. H.; Choi, C. H.; Chung, J. H.; Chung, M. W.; Kim, E. H.; Woo, S. I. Rational Design of a Hierarchical Tin Dendrite Electrode for Efficient Electrochemical Reduction of CO<sub>2</sub>. *ChemSusChem* **2015**, *8*, 3092–3098.

(17) Hu, H.; Gui, L.; Zhou, W.; Sun, J.; Xu, J.; Wang, Q.; He, B.; Zhao, L. Partially reduced Sn/SnO<sub>2</sub> porous hollow fiber: A highly selective, efficient and robust electrocatalyst towards carbon dioxide reduction. *Electrochim. Acta* **2018**, *285*, 70–77.

(18) Wang, M.; Liu, Y.; Xue, D.; Zhang, D.; Yang, H. Preparation of nanoporous tin oxide by electrochemical anodization in alkaline electrolytes. *Electrochim. Acta* **2011**, *56*, 8797–8801.

(19) Ge, H.; Gu, Z.; Han, P.; Shen, H.; Al-Enizi, A. M.; Zhang, L.; Zheng, G. Mesoporous Tin Oxide for Electrocatalytic CO<sub>2</sub> Reduction. *J. Colloid Interface Sci.* **2018**, *531*, 564–569.

(20) Zeng, J.; Nair, J. R.; Chen, Q.; Francia, C.; Bodoardo, S.; Penazzi, N. Cathodes Based on Noncatalyzed Ordered Mesoporous Carbon for Li–O<sub>2</sub> Rechargeable Batteries. *ChemElectroChem* **2014**, *1*, 1382–1387.

(21) Zeng, J.; Francia, C.; Amici, J.; Bodoardo, S.; Penazzi, N. Mesoporous Co<sub>3</sub>O<sub>4</sub> nanocrystals as an effective electro-catalyst for highly reversible Li–O<sub>2</sub> batteries. *J. Power Sources* **2014**, *272*, 1003–1009.

(22) Kim, K.-S.; Kim, W. J.; Lim, H.-K.; Lee, E. K.; Kim, H. Tuned Chemical Bonding Ability of Au at Grain Boundaries for Enhanced Electrochemical CO<sub>2</sub> Reduction. *ACS Catal.* **2016**, *6*, 4443–4448.

(23) Feng, X.; Jiang, K.; Fan, S.; Kanan, M. W. A Direct Grain-Boundary-Activity Correlation for CO Electroreduction on Cu Nanoparticles. *ACS Cent. Sci.* **2016**, *2*, 169–174.

(24) Ottone, C.; Laurenti, M.; Bejtka, K.; Sanginario, A.; Cauda, V. The Effects of the Film Thickness and Roughness in the Anodization Process of Very Thin Aluminum Films. *J. Mater. Sci. Technol.* **2014**, *1* (1), S107.

(25) Lamberti, A.; Garino, N.; Bejtka, K.; Bianco, S.; Stassi, S.; Chiodoni, A.; Pirri, C. F.; Quaglio, M.; et al. Synthesis of ferroelectric BaTiO<sub>3</sub> tube-like arrays by hydrothermal conversion of a vertically aligned TiO<sub>2</sub> nanotube carpet. *New J. Chem.* **2014**, *38*, 2024–2030.

(26) Peercy, P. S.; Morosin, B. Pressure and Temperature Dependences of the Raman-Active Phonons in SnO<sub>2</sub>. *Phys. Rev. B: Solid State* **1973**, *7*, 2779.

(27) Diéguez, A.; Romano-Rodríguez, A.; Vilà, A.; Morante, J. R. The complete Raman spectrum of nanometric SnO<sub>2</sub> particles. *J. Appl. Phys.* **2001**, *90*, 1550–1557.

(28) Lee, B. K.; Jung, E.; Kim, S. H.; Moon, D. C.; Lee, S. S.; Park, B. K.; Hwang, J. H.; Chung, T.-M.; Kim, C. G.; An, K.-S. Physical/chemical properties of tin oxide thin film transistors prepared using plasma-enhanced atomic layer deposition. *Mater. Res. Bull.* **2012**, *47*, 3052–3055.

(29) Lohmann-Richters, F. P.; Abel, B.; Varga, A. In situ determination of the electrochemically active platinum surface area: key to improvement of solid acid fuel cells. *J. Mater. Chem. A* **2018**, *6*, 2700–2707.

(30) Xu, H.; Feng, J.-X.; Tong, Y.-X.; Li, G.-R. Cu<sub>2</sub>O–Cu Hybrid Foams as High-Performance Electrocatalysts for Oxygen Evolution Reaction in Alkaline Media. *ACS Catal.* **2017**, *7*, 986–991.

(31) Li, C. W.; Kanan, M. W. CO<sub>2</sub> Reduction at Low Overpotential on Cu Electrodes Resulting from the Reduction of Thick Cu<sub>2</sub>O Films. *J. Am. Chem. Soc.* **2012**, *134*, 7231–7234.

(32) Baruch, M. F.; Pander, J. E.; White, J. L.; Bocarsly, A. B. Mechanistic Insights into the Reduction of CO<sub>2</sub> on Tin Electrodes Using in Situ ATR-IR Spectroscopy. *ACS Catal.* **2015**, *5*, 3148–3156.

(33) Zeng, J.; Francia, C.; Gerbaldi, C.; Baglio, V.; Specchia, S.; Arico, A. S.; Spinelli, P. Hybrid ordered mesoporous carbons doped with tungsten trioxide as supports for Pt electrocatalysts for methanol oxidation reaction. *Electrochim. Acta* **2013**, *94*, 80–91.

(34) Zeng, J.; Bejtka, K.; Ju, W.; Castellino, M.; Chiodoni, A.; Sacco, A.; Farkhondeh, M. A.; Hernandez, S.; Rentsch, D.; Battaglia, C.; Pirri, C. F. Advanced Cu–Sn foam for selectively converting CO<sub>2</sub> to CO in aqueous solution. *Appl. Catal., B* **2018**, *236*, 475–482.

(35) Sacco, A. Electrochemical impedance spectroscopy as a tool to investigate the electroreduction of carbon dioxide: A short review. *J. CO<sub>2</sub> Util.* **2018**, *27*, 22–31.

(36) Orazem, M. E.; Tribollet, B. *Electrochemical Impedance Spectroscopy*; John Wiley & Sons: Hoboken, USA, 2008.

(37) Ju, W.; Zeng, J.; Bejtka, K.; Ma, H.; Rentsch, D.; Castellino, M.; Sacco, A.; Pirri, C. F.; Battaglia, C. Sn-Decorated Cu for Selective Electrochemical CO<sub>2</sub> to CO Conversion: Precision Architecture beyond Composition Design. *ACS Appl. Energy Mater.* **2019**, *2*, 867–872.

(38) Sacco, A.; Zeng, J.; Bejtka, K.; Chiodoni, A. Modeling of bubble-induced dependent mass transport in the electrochemical reduction of carbon dioxide on nanostructured electrodes. *J. Catal.* **2019**, *372*, 39–48.

(39) Wang, Q.; Dong, H.; Yu, H. Development of rolling tin gas diffusion electrode for carbon dioxide electrochemical reduction to produce formate in aqueous electrolyte. *J. Power Sources* **2014**, *271*, 278–284.

(40) Dutta, A.; Kuzume, A.; Rahaman, M.; Veszteg, S.; Broekmann, P. Monitoring the Chemical State of Catalysts for CO<sub>2</sub> Electroreduction: An In Operando Study. *ACS Catal.* **2015**, *5*, 7498–7502.

(41) Lee, S.; Ocon, J. D.; Son, Y.; Lee, J. Alkaline CO<sub>2</sub> Electrolysis toward Selective and Continuous HCOO<sup>−</sup> Production over SnO<sub>2</sub> Nanocatalysts. *J. Phys. Chem. C* **2015**, *119*, 4884–4890.

(42) Crosa, M.; Boero, V.; Franchini-Angela, M. Determination of Mean Crystallite Dimensions from X-Ray Diffraction Peak Profiles: A Comparative Analysis of Synthetic Hematites. *Clays Clay Miner.* **1999**, *47*, 742–747.

(43) <http://www.xpsfitting.com/search/label/Tin> (accessed November 26, 2018).

(44) Wu, W.-Y.; Chang, Y.-M.; Ting, J.-M. Room-Temperature Synthesis of Single-Crystalline Anatase TiO<sub>2</sub> Nanowires. *Cryst. Growth Des.* **2010**, *10*, 1646–1651.

(45) Elezovic, N. R.; Radmilovic, V. R.; Kovac, J.; Babic, B. M.; Gajic-Krstajic, Lj. M.; Krstajic, N. V. Ptnanoparticles on tin oxide

based support as a beneficial catalyst for oxygen reduction in alkaline solutions. *RSC Adv.* **2015**, *5*, 15923–15929.

(46) Dutta, A.; Kuzume, A.; Kaliginedi, V.; Rahaman, M.; Sinev, I.; Ahmadi, M.; Roldán Cuenya, B.; Veszteg, S.; Broekmann, P. Probing the Chemical State of Tin Oxide NP Catalysts during CO<sub>2</sub> Electroreduction: A Complementary Operando Approach. *Nano Energy* **2018**, *53*, 828–840.

(47) Deng, W.; Zhang, L.; Li, L.; Chen, S.; Hu, C.; Zhao, Z.-J.; Wang, T.; Gong, J. Crucial Role of Surface Hydroxyls on the Activity and Stability in Electrochemical CO<sub>2</sub> Reduction. *J. Am. Chem. Soc.* **2019**, *141*, 2911–2915.

(48) Saravanan, K.; Basdogan, Y.; Dean, J.; Keith, J. A. Computational investigation of CO<sub>2</sub> electroreduction on tin oxide and predictions of Ti, V, Nb and Zr dopants for improved catalysis. *J. Mater. Chem. A* **2017**, *5*, 11756–11763.